Crystal Structures of a Unique Thermal-Stable Thymidylate Synthase from *Bacillus subtilis*[†,‡]

Thomas J. Stout,*[,§] Ute Schellenberger,[||] Daniel V. Santi,[⊥] and Robert M. Stroud*[,§]

Departments of Biochemistry and Biophysics, School of Medicine, University of California, San Francisco, San Francisco, California 94143-0448, and Department of Pharmaceutical Chemistry, University of California, San Francisco, San Francisco, California 94143-0448

Received May 28, 1998; Revised Manuscript Received July 15, 1998

ABSTRACT: Unlike all other organisms studied to date, *Bacillus subtilis* expresses two different thymidylate synthases: bsTS-A and bsTS-B. bsTS-A displays enhanced enzymatic and structural thermal stability uncharacteristic of most TSs. Despite the high level of TS conservation across most species, bsTS-A shares low sequence identity (<40%) with the majority of TSs from other organisms. This TS and the TSs from *Lactococcus lactis* and phage Φ3T—to which it is most similar—have been of interest for some time since, by structure-based sequence alignment, they appear to lack several key residues shown by mutagenesis to be essential to enzymatic function [Greene, P. J., Yu, P. L., Zhao, J., Schiffer, C. A., and Santi, D. (1994) *Protein Sci. 3,* 1114−6]. In addition, bsTS-A demonstrates specific activity 2−3-fold higher than TS from *Lactobacillus casei* or *Escherichia coli*. We have solved the crystal structure of this unusual TS in four crystal forms to a maximum resolution of 1.7 Å. Each of these crystal forms contains either one or two noncrystallographically related dimers. Stabilization of the β-sheet dimer interface through a dramatic architecture of buttressed internal salt bridges maintains the structural integrity of bsTS-A at elevated temperatures. Melting curves of TSs from *L. casei* and *E. coli* are compared to that of TS-A from *B. subtilis* and correlated with numbers of hydrogen bonds, salt bridges, and the numbers of interactions localized to the dimer interface. Analysis of this structure will shed light on the conservation of function across diversity of sequence, as well as provide insights into the thermal stabilization of a highly conserved enzyme.

Enzymes crucial to organism survival tend to be among the more highly conserved across species and are less tolerant of mutational modifications. Studies of enzyme stability and activity have therefore tended to focus on the effects of site-directed mutagenesis of structurally and chemically important residues. Recently, however, with the discovery of extremophiles, there has been increased interest in how organisms can effect proper enzyme stability while maintaining a protein-fold and electrostatic environment conducive to the desired chemical reaction (reviewed in refs *2*−*8*). Clearly, extremophiles have adapted to environmental pressure in order to fill and exploit an available niche. More unusual are mesophiles, organisms living under moderate environmental conditions, which carry macromolecules displaying resistance to extreme conditions. We report to very high-resolution the crystal structure of a highly conserved enzyme, thymidylate synthase (TS),[1] which displays pronounced thermal stability despite its origin from the mesophile *Bacillus subtilis*. The host organism displays the additional unusual feature of carrying genes for two independent thymidylate synthases, TS-A and TS-B. These TSs are distantly related evolutionarily (Figures 1) and display distinct thermal profiles and enzymatic specific activities—providing an "internal standard" for the study of the relationships between protein sequence and structure and the thermal stability and enzymatic efficiency of an enzyme.

All cells synthesize the DNA base thymidine through the conversion of 2′-deoxyuridine monophosphate (dUMP) to 2′-deoxythymidine monophosphate (dTMP). This reductive methylation is catalyzed by the enzyme thymidylate synthase (TS), which—because of its crucial role in nucleotide production—is one of the most conserved enzymes across species and phyla (Figure 1a), as well as being one of the more attractive anticancer drug design targets.

Unlike all other organisms studied to date, *B. subtilis* expresses two separate thymidylate synthases, bsTS-A and bsTS-B. bsTS-B is not expressed or active at temperatures

[†] Supported by the National Institutes of Health (GM24485 and CA-41323 to RMS) and through a postdoctoral fellowship from the American Cancer Society to TJS.

[‡] Coordinates for bsTS-I, bsTS-II, bsTS-III, and bsTS-IV have been deposited with the Brookhaven Protein Data Bank under entry codes 1BKP, 1BKO, 1BSP, and 1BSF, respectively.

* Corresponding authors. E-mail: stroud@msg.ucsf.edu.

[§] Department of Biochemistry and Biophysics.

[||] Current address: Palo Alto Institute of Molecular Medicine, 2462 Wyandotte Street, Mountain View, CA 94043.

[⊥] Department of Pharmaceutical Chemistry.

[1] Abbreviations: TS, thymidylate synthase; dUMP, 2′-deoxyuridine monophosphate; dTMP, 2′-deoxythymidine monophosphate; TS, thymidylate synthase; bsTS, *Bacillus subtilis* thymidylate synthase; ecTS, *Escherichia coli* thymidylate synthase; lcTS, *Lactobacillus casei* thymidylate synthase; DHFR, dihydrofolate reductase; MR, molecular replacement; MIR, multiple isomorphous replacement; NCS, Noncrystallographic symmetry; F_o, observed structure factor; F_c, calculated structure factor; α_{calc}, phases derived from the atomic coordinates.

10.1021/bi981270l CCC: $15.00
Published on Web 09/26/1998

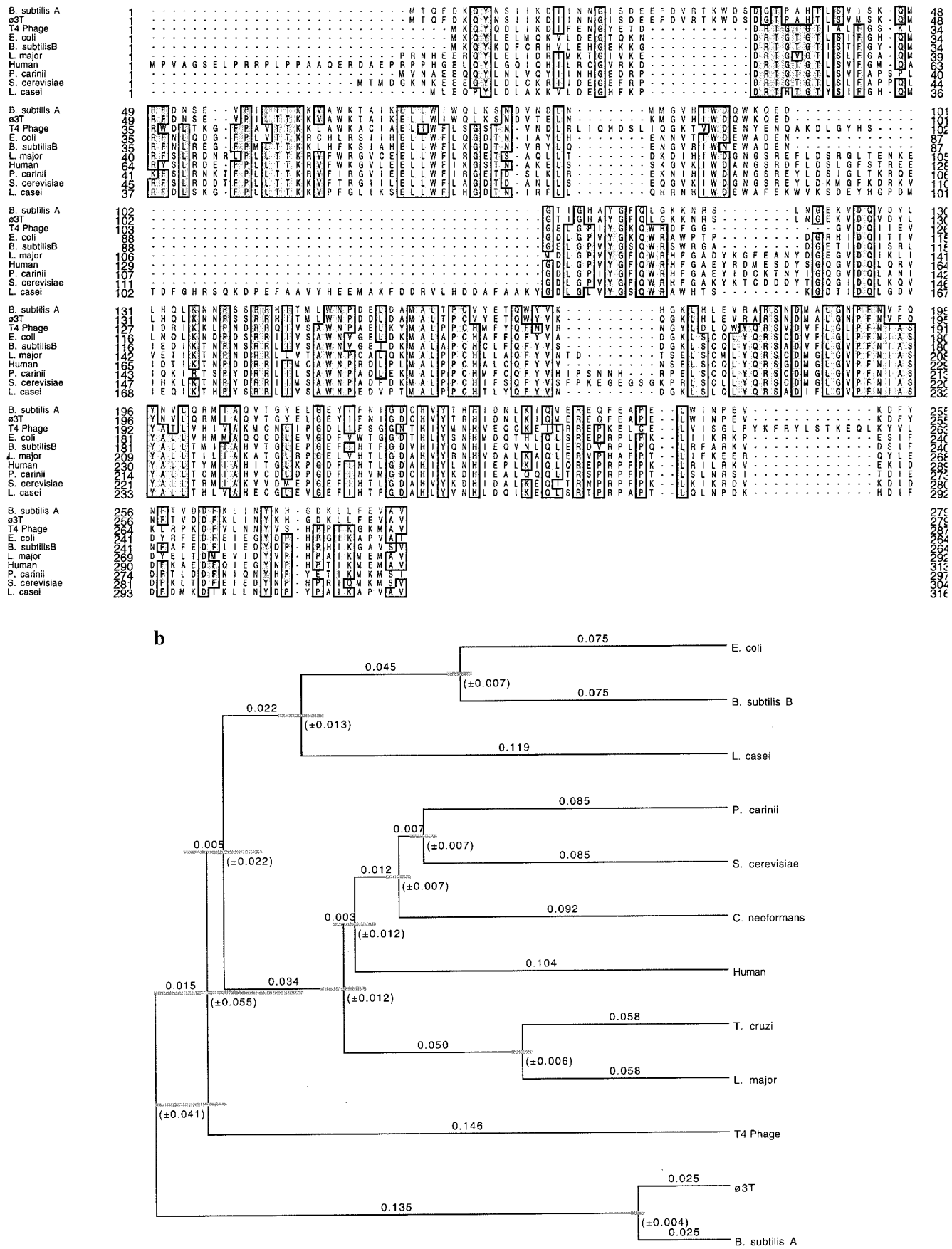

FIGURE 1: (a) Sequence alignment of several selected thymidylate synthases. Shaded boxes correspond to residues which are conserved across at least 8 of the 12 listed sequences. (b) Phylogenetic relationship among selected thymidylate synthases as calculated by GeneWorks based on the alignment in panel a (43). The lengths of the horizontal lines in this figure are proportional to the estimated genetic distance between the sequences, while the numbers at the branch points are the standard error in the position of that branch point.

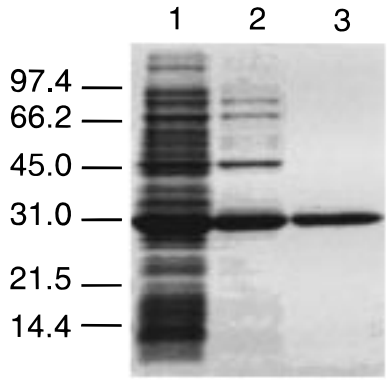

FIGURE 2: Overloaded SDS−PAGE of bsTS-A showing crude lysate (Lane 1), Q-Sepharose purified material (lane 2), and pooled TS-activity containing fractions from phenyl-Sepharose (lane 3).

above 37 °C and accounts for only 5−8% of the total cellular TS activity. bsTS-A displays temperature resistance, allows cells to grow without exogenous thymidine at 46 °C (*9*), and appears to retain structural integrity beyond 65 °C. The two TSs share little sequence identity (38.9%) with one another (Figure 1a). bsTS-B displays a typical TS sequence profile, sharing 64.8% sequence identity (81.8% homology) with TS from *Escherichia coli* and 60.5% sequence identity (74.9% homology) to the enzyme from *Lactobacillus casei*. The other TS expressed by *B. subtilis*, bsTS-A, displays particularly low sequence identity with the majority of previously studied TSs: 37.4% vs *E. coli* (60.3% homology) and 37.2% vs *L. casei* (63.9% homology); however, the enzyme does exhibit 97% sequence identity with the TS from the *B. subtilis* phage, Φ3T (*10*). It remains unclear whether *B. subtilis* possibly incorporated this TS from Φ3T or vice-versa.

Phylogenetically, bsTS-A is one of the more distantly related TSs (Figure 1b) studied structurally to date. Crystal structures have been determined at varying resolutions for the largely conserved TSs from *E. coli* (maximum resolution 1.83 Å) (*11*−*14*), *L. casei* (2.3 Å) (*15*), T4 phage (3.2 Å) (*16*), *L. major* (bifunctional DHFR-TS; 3.2 Å) (*17*), and *H. sapiens* (misfolded; 3.0 Å) (*18*). We report here the three-dimensional structures to a maximum resolution of 1.7 Å of this unusual heat-stable TS from *B. subtilis*. We have shown that bsTS-A consists of two identical subunits, each with a mass of ∼32 813 Da (Figure 2) and that it has an enhanced specific activity relative to previously studied TSs.

MATERIALS AND METHODS

Materials. Plasmid pNHT-1 was a gift from R. Borriss (Humboldt University, Germany) (*10*). This plasmid contains a 3.6 kb *Bcl*I fragment from *Bcl*I digested chromosomal *B. subtilis* 168 DNA that includes the open reading frame of the thyA gene. Expression vector p*Trc* 99A was from Pharmacia. *E. coli* strain DH5α was obtained from Gibco BRL and the Thy$^-$ strain χ2913 (Δthy A572) was provided by R. Thompson (University of Glasgow, U.K.). Restriction endonucleases and T4 DNA ligase were purchased from NEB. Streptomycin sulfate was from Sigma; Q-Sepharose (Fast Flow) and phenyl-Sepharose were from Pharmacia. All other materials were obtained from commercial sources and used without further purification.

Construction of the Expression Vector pTrc-thyA. Plasmid pNHT-1 (*10*) was digested with *Bgl*I and *Xba*I to obtain the 1.6 kb fragment that contains the *thyA* gene. This fragment was gel purified and further digested with *Bsp*HI, which creates an *Nco*I-compatible cloning site at the start codon of the thyA gene. The resulting *Bsp*HI−*Xba*I fragment was ligated into the *Nco*I−*Xba*I sites of expression vector p*Trc* 99A. The ligation mixture was restriction purified by cutting with *Nco*I to select against the parent plasmid (*40*) and transformed into DH5α cells. The resulting plasmid, pTrc-thyA, was verified by restriction analysis. For expression of bsTS-A, plasmid pTrc-thyA was transformed into thymine deficient χ2913 cells.

Protein Purification. Cells were grown in LB medium, supplemented with 100 μg/mL ampicillin and 50 μg/mL thymine. Protein expression was induced at mid-log phase of growth by addition of 1 mM IPTG. After 3 h, the cells were harvested by centrifugation. Cell pellets from 6 L of culture were resuspended in 30 mL of 20 mM Tris, pH 7.4, and 0.1 mM EDTA (buffer A) containing 50 mM KCl and lysed by two passes through a French Pressure cell. Cell debris was removed by centrifugation at 27000*g* for 20 min. High molecular weight nucleic acid was precipitated by addition of 5% streptomycin sulfate (0.12 mL/mL of extract) and removed by centrifugation. The supernatant was loaded onto a Q-Sepharose column (60 mL bed volume, flow rate 1 mL/min), which was preequilibrated with buffer A containing 50 mM KCl. After washing with 200 mL of the same buffer, the protein was eluted with a 600 mL linear gradient from 50 to 500 mM KCl in buffer A. bsTS-A containing fractions were pooled and $(NH_4)_2SO_4$ was added to a final concentration of 1 M. This was loaded onto a phenyl-Sepharose column (70 mL bed volume, flow rate 1.4 mL/min) that was previously equilibrated with buffer A containing 1 M $(NH_4)_2SO_4$. The column was washed with 70 mL of the same buffer, and then a 650 mL gradient from 1 M $(NH_4)_2SO_4$ to 0.6 M $(NH_4)_2SO_4$ in buffer A was applied to elute bsTS-A. The enzyme-containing fractions were pooled and stored at −70 °C.

Enzyme Assay. One unit of bsTS-A activity is the amount of enzyme necessary to produce 1 μmol of product in 1 min. TS activity was measured spectrophotometrically (*41*). The standard assay buffer contained 50 mM TES, pH 7.4, 25 mM $MgCl_2$, 6.5 mM formaldehyde, 1 mM EDTA, and 75 mM β-mercaptoethanol. Both dUMP and (6*R*)-CH_2H_4folate were present at a concentration of 100 μM. Activity assays indicate that bsTS-A has a significantly higher specific activity (SA ≈ 22 units/mg) than either *E. coli* TS (SA ∼13.5 units/mg) or *L. casei* TS (SA ≈ 6 units/mg) when measured using the identical materials and instruments.

Melting Curves. Melting curves were obtained by circular dichroism (CD) using protein at 6−10 mg/mL in 10 mM KPO_4, pH 7.2. Curves were measured between 20 and 90 °C, monitoring 222 nm. Temperature was incremented at 10 °C/h, allowing 3 min equilibration time between measurements. Each of the TSs measured displayed cooperative unfolding, and the melting temperature was determined as the inflection point of the transition curve.

Crystallization. bsTS-A was concentrated to approximately 10 mg/mL during buffer exchange to a final composition of 20 mM Tris, pH 7.4, 0.1 mM EDTA, and 1 mM DTT. The Crystal Screen I incomplete factorial screen

Table 1: Crystallographic Statistics

	bsTS-I	bsTS-II	bsTS-III	bsTS-IV	I−$HgCl_2$	I-pCMB
a	59.94	99.36	57.22	58.99	59.94	59.94
b	81.63	52.83	97.44	96.03	81.63	81.63
c	64.79	129.39	118.02	143.87	64.79	64.79
β	92.52	101.70			92.52	92.52
space group	$P2_1$	$P2_1$	$P2_12_12_1$	$P2_12_12_1$	$P2_1$	$P2_1$
monomers/au	2	4	2	2	2	2
Matthews coefficient	2.42	2.55	2.52	3.12	2.41	2.41
% solvent	48.8	51.3	50.8	60.3	48.8	48.8
resolution (Å)	1.7	2.75	2.2	2.2	2.2	2.1
no. of reflections $\geq 0\sigma$	208 765	80 025	131 066	82 603	42 241	68 589
no. of unique reflections	60 767	31 528	31 172	31 281	32 200	39 918
avg redundancy	3.4	2.5	4.2	2.6	2.2	2.5
R_{symm}[b]	0.086	0.091	0.095	0.084	0.103	0.094
	(0.315)	(0.366)	(0.312)	(0.287)	(0.274)	(0.326)
completeness (%)[b]	88.9 (56.5)	90.9 (81.8)	90.8 (88.8)	23.1 (19.4)	82.6 (72.8)	64.4 (58.2)
R_{merge}[c]					0.153	0.137
R_{cullis}[c]					0.87	0.91
phasing power[d]					0.72	0.68

[a] au, asymmetric unit. [b] The value in parentheses refers to the maximum resolution bin only. $R_{symm} = \sum|I_H - \langle I_H\rangle|/\sum I_H$, where $\langle I_H\rangle$ is the average intensity of the different observations of the reflection, *H*. PCMB, *p*-chloromercury benzoate. [c] $R_{merge} = \sum|F_{PH} - F_P|/\sum F_P$. [d] $R_{cullis} = [\sum|F_{PH} \pm F_P| - F_{H(calc)}|]/(\sum|F_{PH} \pm F_P|)$ for centric reflections. [e] Phasing power $= [\sum F_{H(calc)}^2/\sum F_{PH(obs)} - F_{PH(calc)})^2]^{1/2}$.

from Hampton Research (*19*) was used for preliminary searching of crystallization conditions. Experiments were conducted at 22 °C by the hanging-drop method on silanized cover slips. Fine grid screens of precipitation conditions surrounding promising conditions were used to optimize observed crystal size and morphology.

Data Collection. X-ray diffraction data were collected at room temperature (~20 °C) on an R-Axis IIc imaging plate with a Rigaku RU-200 rotating anode generator operating at 15 kW (50 mA and 300 kV) fitted with a CuK_α anode (λ = 1.5418 Å). The crystal-to-detector distance was 100 mm. Exposures of 20 min/1° oscillation range were used throughout the data collections, with the exception of bsTS-I which was collected at 15 min/1° oscillation. The diffraction data were indexed, integrated, scaled, and merged with the HKL software package (*42*). A summary of the data processing statistics is presented in Table 1.

RESULTS AND DISCUSSION

Overexpression and Purification. bsTS-A was successfully overexpressed to high levels in *E. coli*, producing ~50 mg of bsTS-A/L of cell culture. A two-step purification scheme involving ion-exchange chromatography, followed by hydrophobic chromatography, was successfully employed to purify the enzyme to homogeneity as visualized by overloaded SDS−PAGE (Figure 2). Activity assays indicate that bsTS-A has a significantly higher specific activity (SA ≈ 22 units/mg) than either *E. coli* TS (SA ~13.5 units/mg) or *L. casei* TS (SA ≈ 6 units/mg) when measured using the identical materials and instruments.

Crystallization and Characterization. bsTS-A was concentrated to 10 mg/mL during buffer exchange against 20 mM KPO_4, pH 7.0. Small crystals of bsTS-A were observed within 1 h in experiments at room temperature against an incomplete factorial screening kit, Crystal Screen I (*19, 20*), in condition numbers 6, 10, 14, 15, 18, 20, 22, 23, 28, and 32, with the most promising leads appearing in condition numbers 14 and 15 (*21*). Both single-crystal size and morphological quality were optimized by fine screening of conditions 14 and 15 at 30 and 32% dilutions with water of the initial precipitant concentrations, respectively.

Crystals from condition no. 15 were found to belong to four distinct crystal forms, all of which could be found in varying proportions in the same drops. Of these four crystal forms, two belong to the monoclinic space group $P2_1$ and two to the orthorhombic space group $P2_12_12_1$. The respective unit cell dimensions and asymmetric unit contents are summarized in Table 1.

Form I of these crystals, referred to as bsTS-I, diffracts to beyond 1.7 Å using an in-house rotating anode radiation source, and has unit cell dimensions of a = 59.94 Å, b = 81.63 Å, c = 64.79 Å, and β = 92.52°. The diffraction maxima show intensity statistics consistent with the space group $P2_1$. Additional analysis of these data indicated that the asymmetric unit contains a full dimer of bsTS-A, with relatively strong noncrystallographic symmetry (75.5% of the origin peak height on a self-rotation map) between the two monomers (Φ = 42.0°, Ψ = 90.0°, κ = 180 ± 0.1°; self-rotation data not shown). The presence of this noncrystallographic 2-fold is consistent with the calculated protein density of 2.42 $Å^3$/Da which indicates an approximate solvent content of 49%, well within the usual range expected for crystals of globular proteins (*22*).

Crystals of form II, referred to as bsTS-II, diffract to a maximum resolution[2] of 2.75 Å, and also belong to the monoclinic space group $P2_1$; however, the asymmetric unit contains two complete dimers. This has been confirmed by the presence of noncrystallographic symmetry elements relating each of the four monomers ($\kappa_{1,2}$ = 179.7°, $\kappa_{1,3}$ = 177.4°, $\kappa_{1,4}$ = 165.9°; self-rotation data not shown). The unit cell constants are a = 99.36 Å, b = 52.83 Å, c = 129.39 Å, β = 101.70°; corresponding to an approximate doubling of the c axis relative to the bsTS-I crystal form.

Forms III and IV belong to the orthorhombic space group $P2_12_12_1$, and each contains one complete dimer in the asymmetric unit, however, form IV is ~25 Å longer than form III along the *c*-axis. This corresponds to an ~10%

[2] Defined by applying an $I/\sigma(I) \geq 3.0$ cutoff.

Scheme 1: Structure Solution Schematic Showing the Interplay of the Multiple Crystal Forms and Crystallographic Methods Used in the Solution of the bsTS-A Crystal Structures

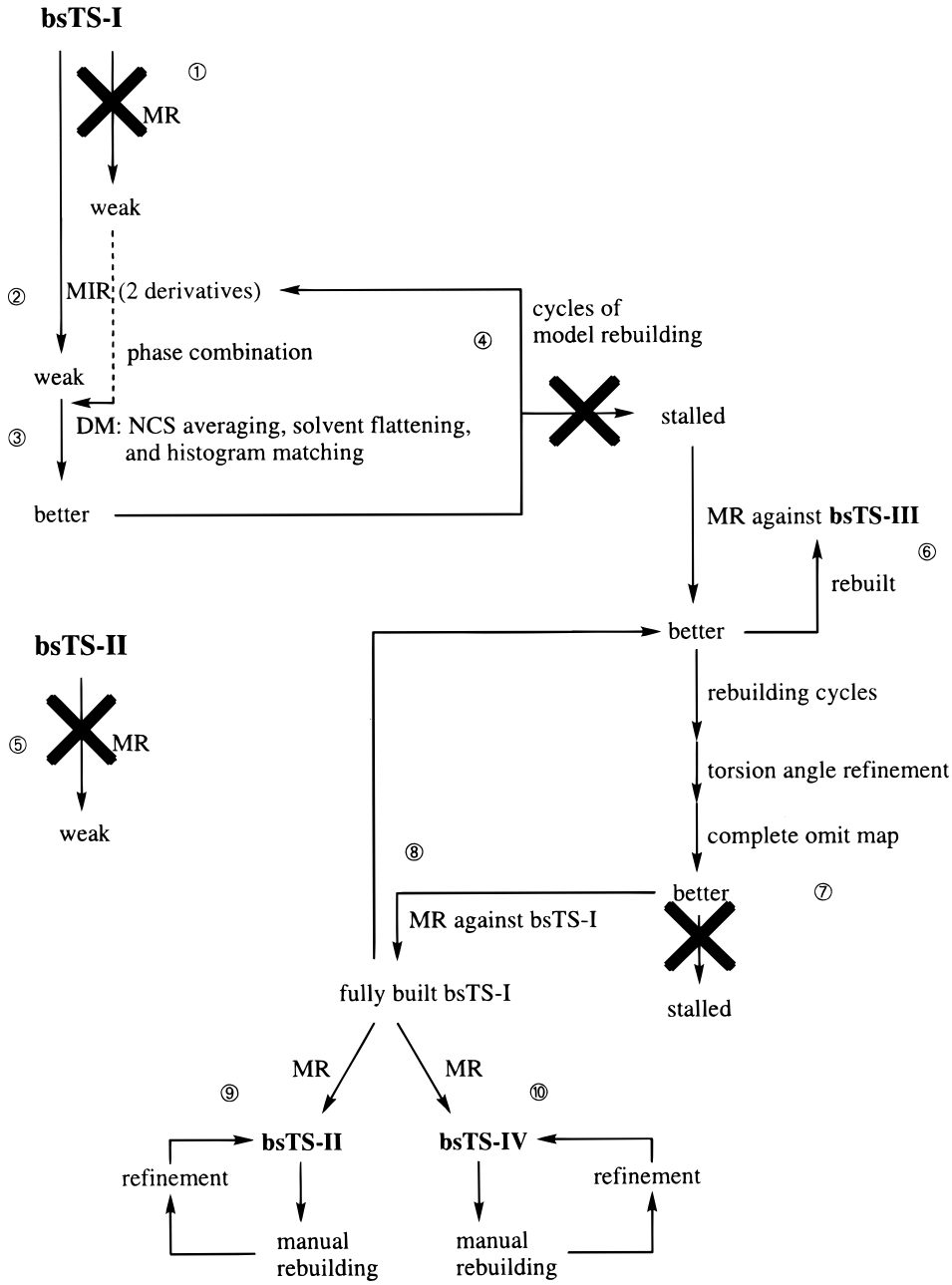

increase in solvent content, and these crystals decay rapidly in the X-ray beam. bsTS-III crystals, however, are quite stable, and diffract well to high resolution. Interestingly, forms I and II exhibit the same morphology (irregular plates) and are visually indistinguishable, while forms III and IV grow as rectangular parallelepipeds and needles, respectively.

Structure Solution. The three-dimensional structure of bsTS-A in each of these crystal forms has been solved by a combination of crystallographic techniques including multiple isomorphous replacement (MIR), molecular replacement (MR), and the electron density modification techniques of noncrystallographic symmetry averaging (*23*, *24*), solvent flattening and histogram matching (*25*, *26*) among the four crystal forms of bsTS-A. A schematic of this process is presented in Scheme 1. Each of the major steps in the structure determination process has been numbered, and will be briefly discussed in succession.

1. Following collection of the high-resolution bsTS-I data, molecular replacement was immediately attempted using models of *E. coli* TS (ecTS), which although distant at 37.4% sequence identity, is the most closely related TS whose three-dimensional structure has been solved. Models which were used as search probes included (1) a complete dimer of apo-ecTS (PDB entry 1TJS) with all solvent and ligand atoms removed, (2) a dimer of ecTS without solvent or ligands and all side chains truncated to alanine (Gly intact), (3) a dimer of ecTS without solvent or ligands and all side chains truncated to serine (Gly intact), (4−6) monomers of models 1−3, (7−9) models 4−6 with loops removed, (10−12) models 1−3 with loops removed, and (13) a homology model built based on the *E. coli* TS crystal structure with loops removed as in models 7−9, conserved side chains retained, and point mutations modeled based on the greatest extent of the *E. coli* side-chain rotomer or the most likely conformer

based on local packing. To produce model 13, a complete dimer was generated by applying a pure 2-fold rotation [as crystallographically observed in apo-ecTS (1TJS) after the modeling had been carried out on the monomer. All 13 models were used as molecular replacement probes in both AMoRe (*27*) and X-PLOR (*28*). Only model 13 showed a rotation search signal which was sufficiently above the noise level to proceed with searching against the translation function (or Patterson-correlation refinement in the case of X-PLOR). Even with model 13, the solution could at best be considered weak, with the top solution just 1.5σ above the first noise peak. Electron density maps calculated using this model were not readily interpretable. There was reasonable density for the interior β-sheet region, but additional density for the unmodeled portions of the structure could not be obtained even with the density modification techniques of NCS averaging (*23*), solvent flattening, and histogram matching (*25*, *26*).

2. Simultaneous with step 1, isomorphous heavy-atom derivatives of bsTS-I were sought. Successful isomorphous derivatives were obtained by soaking crystals of bsTS-I for 15−18 h in either 1 mM $HgCl_2$ or 1 mM *p*-chloro mercury benzoate (pCMB). Both derivatives were solved by the difference Patterson technique, refined, and cross-phased. Statistics for each are presented in Table 1. Both mercurials shared a common site—covalently attached to the active-site cysteine—and the smaller mercurial ($HgCl_2$) also fully occupied a site approximately 7 Å away. The fully built and refined structure shows this to be the location of an additional buried cysteine without direct access to the active site. Initial MIR phased maps were not readily interpretable; however, NCS averaging (*23*) and solvent modulation (*25*, *26*) improved the quality of the electron density considerably. The region of space corresponding to the dimer interface, which was also closest to the NCS operator, could be seen to be β-sheet. However, with increasing distance from this operator, the quality of the density diminished rapidly, and these phases were not adequate for model building.

3. While neither methods 1 or 2 were independently successful, they each provided phase information regarding the structure, so phase combination was used to maximize the quality of the electron density maps. Indeed, these maps retained the quality of the interior β-sheet density seen from the molecular replacement solution, as well as additional information regarding portions of the structure not included in the molecular replacement model. These maps were further improved through the application of NCS 2-fold averaging, solvent flipping, and histogram matching (*25*).

4. Multiple rounds of manual model rebuilding were interleaved with recomputation of the above-mentioned phase combination and density modification procedures to extend the portion of the structure which could be accounted for in the model. Initial cycles showed obvious improvement in the density for the portions of the structure modeled and yielded additional stretches of new density; however, this boot-strapping stalled after approximately 5 rounds of model rebuilding (with approximately 60% of the mainchain residues modeled, and 30% of these residues modeled only as alanine) and no further information could be obtained from the available model-based and experimental phases.

5. During heavy-atom derivative searching, a second crystal form, morphologically identical to bsTS-I, was found and native data were collected for bsTS-II. After the forward progression of model building in bsTS-I stalled, molecular replacement was attempted against bsTS-II using the current bsTS-I model as well as the homology model (no. 13). Neither of these MR attempts were successful, most likely due to the inherent phase error of an incomplete, partially incorrect search model as well as the reduced signal-to-noise ratio since this crystal form contains 4 monomers/asymmetric unit.

6. During heavy-atom screening of forms bsTS-I and bsTS-II, a crystal of one of the other morphologies was examined and found to diffract well. These crystals were in fact yet another crystal form, and native data for bsTS-III were collected and examined as another molecular replacement target. The unit cell was found to belong to the orthorhombic Bravais lattice, with $a = 57.22$ Å, $b = 97.44$ Å, $c = 118.02$ Å. The space group was $P2_12_12_1$. It was hoped that since these crystals were orthorhombic, with equivalent symmetry elements in all three orthonormal directions throughout the lattice, perhaps the structure factor relationships would be sufficiently different from those in bsTS-I and bsTS-II to assist in further solution of the bsTS structure. This, in fact, turned out to be the case. Molecular replacement using the current bsTS-I model gave two unique solutions (10σ above the first noise peak) related by an NCS 2-fold.

7. Initial electron density maps of bsTS-III contained more density in the missing regions of the model than had been observed in bsTS-I; however, these sections were not easily interpretable. Many cycles of manual building alternated with positional refinement, and simulated annealing protocols gave considerable improvement; however, certain portions of the structure showed weak and broken density, while several loops remained undefined. Application of torsion angle refinement (*29*) greatly enhanced the accuracy of the structural portions built in the previous step. This resulted in small shifts of the main chain throughout the newly built regions (<0.5 Å rms) but a substantial increase in the quality of the local electron density, as well as in regions for as yet unbuilt portions of the structure—particularly in the remaining unbuilt loop regions. This refinement protocol, in combination with a "complete composite simulated annealing omit map" (*30*) calculated for the entire protein, allowed extensive building of the remaining portions of the structure. However, this procedure also stalled with several extensive loops remaining undefined; in particular the region from 23 to 42 was not observed in either monomer with sufficient density to allow an unambiguous tracing of the protein chain.

8. At this stage, since the model was substantially advanced since step 1, molecular replacement was reperformed against the high-quality bsTS-I data using the current bsTS-III model as a search probe. This search was unambiguously successful, yielding only one solution. At this stage, final construction of the bsTS-I structure proceeded quickly, with clear density visible for all of the remaining unbuilt loops. Refinement and manual rebuilding then proceeded to solidify side-chain rotomers and increase the employed resolution to the 1.7 Å limit. Once the entire bsTS-I structure was built prior to the modeling of any solvent molecules, the entire chain trace and side-chain orientations were confirmed with a complete omit map. Waters were then built into difference density ($F_o - F_c$) that

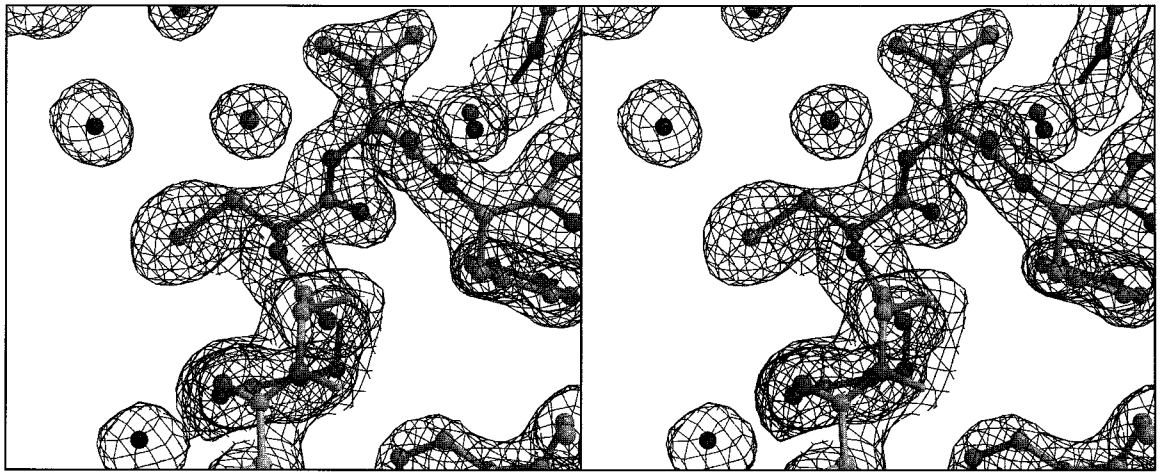

FIGURE 3: Final, refined electron density (using coefficients $3F_o - 2F_c$ and phases α_{calc}) for bsTS-I at 1.7 Å; Figures 3−7 were created using Molscript (*45*) and Raster3D (*46*−*48*).

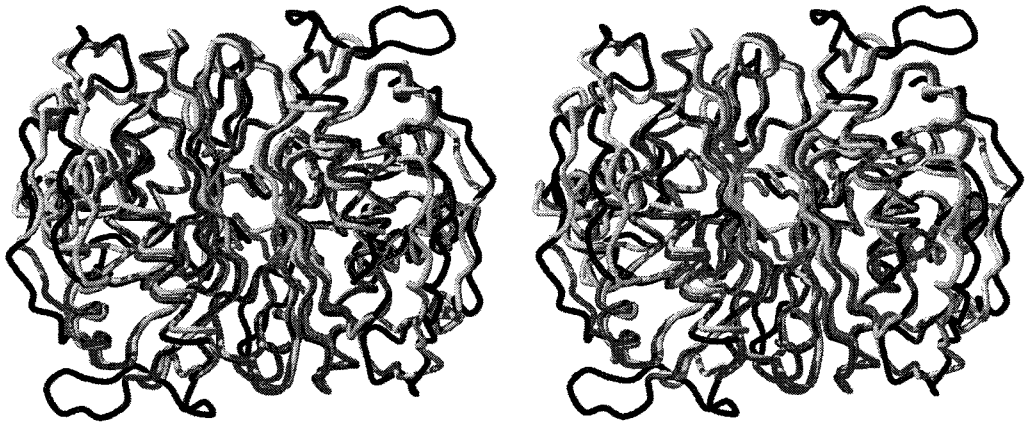

FIGURE 4: Superposition of bsTS-I with apo-*E. coli* TS (1TJS). *E. coli* TS is shown in white; bsTS-I is shown in gray for the core region (those portions which deviate from *E. coli* TS by <3.6 Å rmsd) and in black for those portions which are unique and/or deviate by >3.6 Å rmsd.

was at least 3.5σ, and displayed good stereochemical criteria for at least one hydrogen bond to the protein or bridging solvent molecules. A representative portion of the final, refined electron density for the region surrounding the catalytic cysteine is shown in Figure 3.

9 and 10. With a completed bsTS structure in hand, the other crystal forms (bsTS-II and bsTS-IV) were subsequently solved through straightforward molecular replacement. Each form displayed some structural differences which were quickly identified and rebuilt. These are discussed further below. Due to the reduced resolution (bsTS-II) or completeness (bsTS-IV) of these data sets relative to bsTS-I and bsTS-III, strict NCS constraints were maintained throughout these refinements.

Structure of TS-A from B. subtilis. TS-A from *B. subtilis* is an obligate dimer of mixed $\alpha-\beta$ fold, similar to previously studied TSs (*12*, *15*−*18*). The central β-pleated sheet forms the extensive dimer interface, burying 2,235 Å^2 of surface area (−21 Å^2 vs. *E. coli*; −388 Å^2 vs. *L. casei*). While the rms deviations (Table 2) on the coordinates of conserved structural components of TSs whose crystal structures have been solved are relatively large (indicating a disparity of structure), topologically, bsTS-A is very similar to other TSs. As has been found with TSs from other species (*13*), while the overall fold and arrangement of secondary structural elements is retained, variation in amino acid composition leads to plasticity of conformation. In other words, while the sequential arrangement of secondary structural elements retains the "TS-fold", there are significant shifts found in the relative orientations of these elements.

Table 2: Alignment Among Known TS Crystal Structures

	no. of C_α core atoms	rmsd (Å) vs bsTS-I
E. coli	487	1.33
L. casei	483	1.55
T4 phage	441	1.52

In addition to the conserved secondary structural elements found within the canonical TS-fold, thymidylate synthase A from *B. subtilis* shows several additional secondary structural features. In particular, the insertion from 24 to 33 (*B. subtilis*-A numbering) forms a modified strand-turn-strand mini-β-sheet which is extended to the C-terminal residue (V279). This interaction creates a three-dimensional localization of the C-terminus deeper within the active-site cavity than is generally seen in apo-TS structures. With the exception of TS from T4-phage,[3] unliganded structures of TSs have previously shown the C-terminus to be in an open

[3] TS from T4-phage also has an anomalously high specific activity (*31*, *32*).

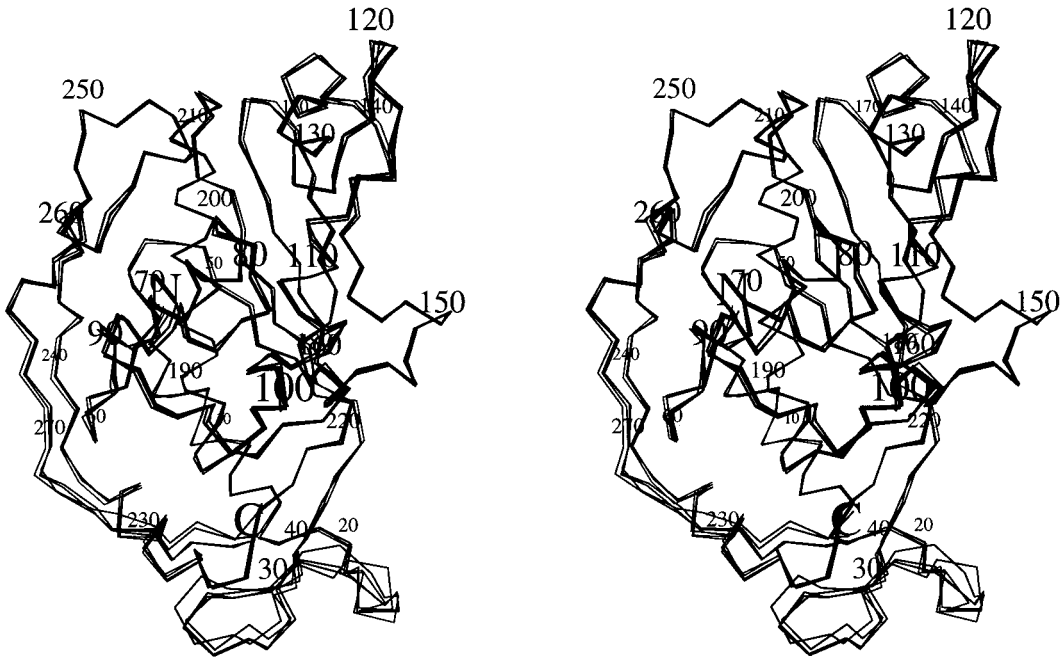

FIGURE 5: Convergent stereoview of the superposition of monomers from each of the four crystal forms: bsTS-I, bsTS-II, bsTS-III, and bsTS-IV. Every tenth residue is numbered, and the N- and C- terminii are labeled. While largely conserved, there are regions of notable variations, particularly at the south end of the molecule. This region of bsTS involves the catalytically imperative C-terminus as well as the loop insertion from residues 20−40 (see Figure 1).

conformation, withdrawn from the active site and not specifically interacting with any portion of the enzyme. The strong interactions between the 20s loop of bsTS-A and the mainchain of the C-terminal residue may well account for the enhanced specific activity of this enzyme relative to previously studied TSs.[4] By localizing the C-terminus, it becomes preordered through a reduction in local entropy and a lower energy barrier must be surmounted in the transition from the open form to the catalytically competent or closed form, potentially leading to the observed enhancement in the rate of enzymatic turnover.

Structure of bsTS-A among Four Crystal forms. Comparison of the structure of the bsTS-A polypeptide determined in four different crystal forms shows two specific regions of significant difference in the main-chain conformations among these crystal forms (Figure 5). The loop from 115 to 125 (100−110 in *E. coli*) not only differs significantly in conformation from the orientation found in previously studied TS crystal structures, but also displays shifts of up to 1 Å in main-chain coordinates between the four crystal forms of bsTS-A. This is likely due to differing crystal-packing forces which have selected for alternate side-chain rotamers and interactions of this exposed loop with both ordered and mobile solvent. For example, in polymorphs bsTS-I and -III this loop forms extensive crystal contacts with symmetry related molecules, while in polymorphs bsTS-II and -IV, there are no crystal contacts to this exposed loop. Perhaps not coincidentally, this trend also corresponds with the percent solvent content of these crystal forms and the inherent quality of the diffraction data. The region which differs most significantly among the polymorphs of bsTS-A involves the C-terminus and the insertion from residues 24 to 33. Among the four crystal forms studied, three very different conformations for this region have been found. It is interesting to note that while the structure of the 20s loop and the C-terminus differs in each polymorph, the interaction between the two short strands and the C-terminal residue is maintained in all but bsTS-II. It is this polymorph which contains a phosphate counterion in the nucleotide-binding pocket of the active site. This is discussed in greater detail below; however, it appears that there may be structural evidence among these crystal structures for an equilibrium between the open form of the enzyme (where the C-terminus is held out of the active site by its interactions with the 20s loop) and a ligand-bound conformation where a phosphate-bearing substrate draws the C-terminus into the active site.

Phosphate Binding. All crystal structures of thymidylate synthases previously studied have shown the presence of either substrate, substrate analogues, or a phosphate/sulfate ion in the active site. This ion, and the phosphate of substrate-like ligands, is coordinated by four absolutely conserved arginines, and efforts to produce empty active-site crystal structures have not been previously successful. bsTS-A is of interest since structure-based sequence alignments have suggested that one of these four conserved arginines appears to be absent (*1*). The crystal structures of bsTS-A in four crystal forms show that this region of the active site in fact does contain four arginines; the loop insertion from 24 to 33 contributes an arginine at position 28, which roughly approximates the spatial location of the arginine in question from previous sequence alignments. It also appears, however, that this arginine is not likely to play as strong a role in the binding and localization of the nucleotide phosphate as is the case in other TS structures. The unique architecture of the 20s loop results in a notable shift of this arginine out of the phosphate-binding pocket by an average of 4.3 Å relative to the α-carbons of the corresponding arginines in the *E. coli*, *L. casei*, and T4 phage

[4] Specific activities for TS from several species: bsTS-A, 22 units/mg; ecTS, 13.5 units/mg; lcTS, 6 units/mg.

Table 3: Refinement Statistics

	bsTS-I	bsTS-II	bsTS-III	bsTS-IV
resolution limits (Å)	48.3−1.7	30.0−2.75	8−2.5	60.0−2.20
no. of reflections (2σ)	60 736	31 528	19 881	8859[a]
refined *R*-factor (%)[b]	15.1	21.4	18.1	19.5
Free *R*-factor (%)	20.6	31.9	26.0	30.1
rmsd bond lengths (Å)	0.006	0.007	0.006	0.007
rmsd bond angles (deg)	1.3	1.3	1.3	1.2
rmsd improper angles (deg)	1.11	1.17	1.15	0.60
rmsd dihedral angles (deg)	24.2	24.4	24.6	27.6
est coord error (Luzzati)	0.16	0.33	0.24	0.27
est coord error (SIGMAA)	0.16	0.45	0.23	0.34
no. of protein atoms	4602	9204	4610	2,301
no. of water molecules	350	35	113	0
$\langle B \rangle$ overall (Å^2)	24.9	17.9	26.2	22.8
$\langle B \rangle$ per monomer (Å^2)	23.3; 24.2	16.1; 18.5; 19.2; 17.6	27.9; 24.0	NCS
$\langle B \rangle$ solvent (Å^2)	40.1	30.9	35.13	
$\langle B \rangle$ heterogens (Å^2)			61.15	

[a] $\geq 0\sigma$. [b] *R*-factor $= \sum|F_{obs} - F_{calc}|/\Sigma F_{obs}$.

TS crystal structures. The result of this disruption of the outer wall of the active site results in a reduced affinity for the phosphate moiety, at least under crystallization conditions.[5] Of the 10 active sites observed in the four bsTS crystal forms, only two contained a PO_4^{2-} or SO_4^{2-} ion, despite all of the crystals having been grown under identical conditions containing phosphate buffer and ammonium sulfate. In the only crystal form which does contain a counterion in the active site—bsTS-II—the ion is somewhat poorly ordered, indicating local mobility or reduced occupancy. Surprisingly, the other crystal forms (bsTS-I, -III, -IV) contain no crystallographically detectable ligand binding at this site; difference Fourier density maps do not indicate any ordered solvent or counterions within 5 Å of the phosphate-binding site. This reduced affinity for phosphate binding in the active site of bsTS-A is directly related to the reorganization of one wall of the active site in the region of the unique loop insertion from E24 to S33 and may contribute to the increased specific activity of this enzyme through more facile product release.

Comparison of bsTS-A to Other TSs. Comparisons of TS-A from *B. subtilis* to thymidylate synthase from other species were made using bsTS-I, the crystal form which diffracts to highest resolution. The dimers were superimposed using C_αs of a nonvariant core defined by C_αs which deviate by less than 2.5 Å from an aligned partner atom (*35*, *36*).

Superposition of the crystal structure of bsTS-I and *E. coli* TS (Figure 4) gives a root-mean-square deviation of 1.33 Å based on 487 common core α-carbons. These two enzymes are the most conserved, both spatially and in sequence homology, among the TSs for which crystal structures have been determined. The best-aligned core—indicated in gray in Figure 4 — lies in the β-sheet and portions of the adjacent α-helices.

Structural Basis for Thermal Stability. The structures of a number of thermophilic macromolecular structures have been determined and comparisons to mesophilic homologues made (selective references: refs *6* and *7*). It is becoming clear that thermostability is achieved by a variety of means, including: (*i*) internal cores which are significantly more hydrophobic in composition than their mesophilic counterparts (thus disfavoring unfolding events which would expose the core to solvent), (*ii*) sequences containing more hydrogen bonds, salt bridges and disulfide bonds (anchoring the native fold against the increased kinetic motions at elevated temperatures), and—most commonly—(*iii*) some mixture of these strategies. In the case of bsTS-A, which is unusual among heat stable enzymes since *B. subtilis* is a mesophile, this stabilization is accomplished through a dramatic arrangement of a large number of internal salt bridges bracing the dimer interface (Figure 6), described in detail in Table 4.

To address the question of the numbers of salt bridges versus heat stabilization in various TSs, melting curves were obtained for the TSs for which crystal structures have been

Table 4: Salt Bridge Partners in bsTS-I

intermonomeric salt bridges		distance (Å)	XX-X-Y[a] (deg)	X-Y-YY[a] (deg)
Lys 114 N_ζ	Asp 451 $O_\delta 2$	2.71	109.2	113.4
Arg 117 $N_\eta 2$	Asp 454 $O_\delta 1$	2.78	110.0	156.3
Arg 141 N_ϵ	Asp 520 $O_\delta 2$	3.18	138.4	123.1
Asp 151 $O_\delta 2$	Lys 414 N_ζ	2.82	106.9	120.5
Asp 154 $O_\delta 1$	Arg 417 N_ϵ	3.12	108.0	103.8
Lys 170 N_ζ	Asp 520 $O_\delta 1$	2.91	107.4	159.0
His 171 $N_\delta 1$	Glu 324 $O_\epsilon 2$	3.29	115.4	97.8
Glu 177 $O_\epsilon 1$	Arg 479 $N_\eta 2$	2.88	106.3	142.3
Arg 179 $N_\eta 2$	Glu 477 $O_\epsilon 1$	2.89	141.1	107.7
Asp 220 $O_\delta 2$	Lys 470 N_ζ	2.91	146.2	111.9
intramonomeric salt bridges (duplicated in second monomer)				
Asp 14 $O_\delta 2$	Lys 46 N_ζ	2.82	108.8	88.6
Asp 22 $O_\delta 1$	His 39 $N_\delta 1$	3.13	122.0	151.4
Asp 34 $O_\delta 1$	Arg 226 $N_\eta 1$	3.41	93.2	102.3
Asp 34 $O_\delta 2$	Arg 226 $N_\eta 2$	2.71	121.5	115.7
Arg 49 N_ϵ	Glu 213 $O_\epsilon 2$	2.84	118.2	111.7
Arg 49 $N_\eta 2$	Glu 213 $O_\epsilon 1$	3.07	119.0	100.9
Lys 79 N_ζ	Asp 125 $O_\delta 2$	2.90	115.9	115.1
His 92 $N_\delta 1$	Asp 95 $O_\delta 2$	2.89	146.1	124.4
His 106 $N_\delta 1$	Glu 152 $O_\epsilon 2$[b]	2.98	117.0	111.7
Lys 114 N_ζ[b]	Glu 152 $O_\epsilon 1$[b]	2.85	130.2	99.5
Lys 115 N_ζ	Asp 125 $O_\delta 2$	3.10	104.6	129.4

[a] X and Y are the directly interacting partners indicated in the table; XX and YY are the first covalently bonded atom of the respective partner in the direction of that residue's α carbon. [b] Intramonomeric salt bridge partners that are also directly involved in intermonomeric salt bridges.

[5] The R23I mutation in *Lactobacillus casei* TS results in a 25-fold elevated K_d for the substrate, dUMP (*33*, *34*).

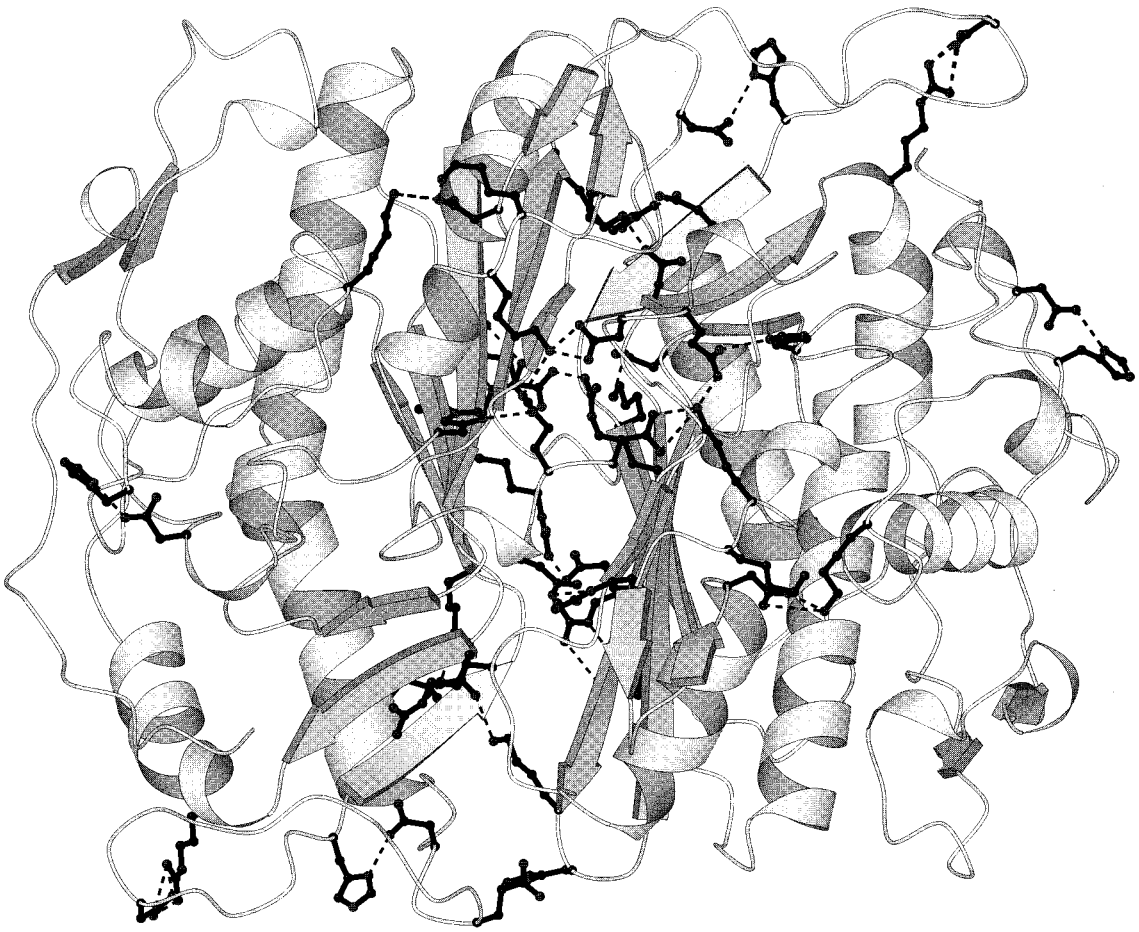

FIGURE 6: Salt bridges in bsTS. The majority involve partners from opposite monomers spanning the dimer interface; all but two of the remainder are directly connected to the intermonomeric salt bridges by buttressing hydrogen bonds. The side chains involved are shown in black ball-and-stick representation; the salt bridges and hydrogen bonds are depicted with dashed lines.

Table 5: Relationship between the Number of Salt Bridges in TS and Melting Temperature

species	melting temperature (°C)	no. of salt bridges (dimer)	no. of salt bridges (interface)[a]	monomer surface buried (Å^2)
L. casei	37.8	8	2	2623
E. coli	45.7	10	2	2256
B. subtilis (A)	68.9	20	11	2235

[a] Interfacial salt bridges are those which include one partner from each monomer at the dimer interface.

determined and which were readily accessible. Thermal denaturation was monitored by circular dichroism (CD) under identical conditions for each of the TSs from *L. casei*, *E. coli*, and *B. subtilis* (A). A table of the melting temperature (T_m) versus the numbers of salt bridges in each structure is presented in Table 5. Here, a clear trend is seen, not only for the total number of salt bridges present and thermal stabilization, but in particular for the number of salt bridges crossing the dimer interface. This is in contrast to the amount of surface area buried by the dimer interface for each of these TSs which remains largely invariant across all of the TS structures determined to date (Table 5). A particular exception to the maxim of stabilization via surface area buried is the TS from *L. casei*, which buries nearly 400 Å^2 more surface area due to the large insertion from residues 85−132. Yet, this enzyme displays the lowest thermal stability of the TSs that have been studied. It seems clear that bsTS-A obtains its thermal stability from these internal salt bridges which serve to stabilize the dimer interface. A closer look at the salt bridges which do not cross the dimer interface shows a remarkable arrangement whereby all but two are, in fact, hydrogen-bonding partners with the salt bridges which do cross the dimer interface. The role of these "second tier" salt-bridges appears to be as buttressing partners to the interfacial salt bridges, further stabilizing that interface. Therefore, 18 out of 20 salt bridges are directly or indirectly involved in stabilizing monomer/monomer contact, leaving just two independent salt bridges involved in stabilizing the geometry of external loops.

In addition to these sequence adaptations, several completely conserved residues which have been thought to play key roles in the enzymatic mechanism of the TS reaction are also modified. These residue modifications have previously been proposed on the basis of modeling studies to be covariantly conserved through three-dimensional functional accommodation (*1*). One of these, arginine 23 (*L. casei* numbering), is structurally conserved, although it is found in a loop insertion (Arg 28, bsTS-A numbering) unique to the bsTS-A, *L. lactis*, and phage Φ3T TS sequences. The presence of this component of the phosphate-binding site on a sequentially divergent loop places the side chain of R28 considerably farther from the phosphate site than has been observed in previous TS crystal structures. This relaxation of the phosphate-binding site may account for the reduced

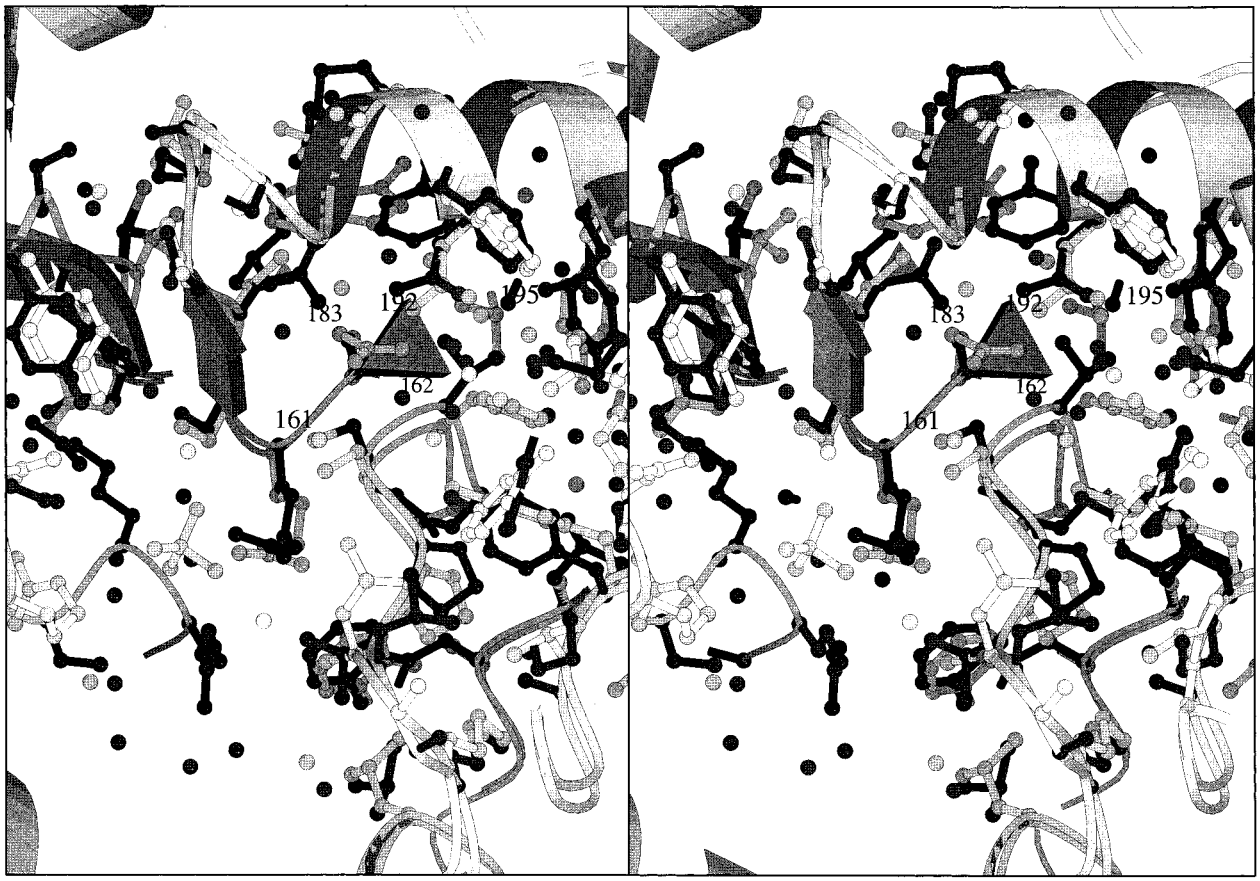

FIGURE 7: Convergent stereoview of some of the important differences in the active site of *B. subtilis* TS-A (black side chains) relative to the active site of *E. coli* TS (light gray side chains), which is representative of the main body of largely conserved TSs. The superposition was performed on the basis of optimizing the root-mean-square deviation of the subset of C-α pairs which fall within 2.5 Å of one another. Important differences include His147(199) → V162, Ser180(232) → Q195; Ser168(220) → N183, where the initial residue is that found in the family of strictly conserved TSs using *E. coli* (*L. casei*) numbering and the residue found in bsTS-A is listed second. Within the figure, labeled residues include the catalytic cysteine (161), V162, N183, N192, and Q195. Note that where the PO_4^{2-} is bound in the *E. coli* structure, only a water is found in the polymorphs bsTS-I, -II, and -IV. A poorly ordered PO_4^{2-} is found in this site in bsTS-III. All of these crystal forms were found in the same crystallization samples.

ordering of counterions in the four crystal structures studied here. In three of the crystal forms, a phosphate ion cannot be located in the active site, despite the high quality of most of these structures and diffraction data. In the one crystal form in which PO_4^{2-} is clearly present, bsTS-III, the ion is apparently not well anchored. This is reflected in thermal parameters which are nearly twice those of the surrounding protein residues, and most likely reflects a reduced binding affinity for PO_4^{2-} in this active site.

Another predominantly conserved residue which differs in the bsTS-A structure is His199,[6] found as a valine in bsTS-A. This residue is immediately C-terminal to the catalytic cysteine and plays a role in ordering the catalytic water structure. Systematic mutagenesis of His199 has found several mutants which retain activity, but in all cases, the catalytic activity was reduced at least 10-fold (*37*−*39*). Greene et al. (*1*) have proposed that Ser232 (Gln195 in bsTS-A) takes over the function of the missing histidine in coordinating the water structure which is thought to stabilize an iminium ion formed in the course of the enzymatic reaction. The crystal structure does not fully support this proposal, however, as Q195 is located too far from the position of the structural water which is coordinated by the conserved histidine to exert any complementary effect (Figure 7). Analysis of the structure of the bsTS-A active site (Figure 7) indicates that it is more likely the presence of an additional asparagine in the active site, located at N183 (Ser168 in *E. coli*; Ala220 in *L. casei*) which pushes N192 (N177, *E. coli*; N229, *L. casei*) into a conformation which compensates for the missing histidine. This is merely a proposal, however, and requires the determination of bsTS-A in complex with substrates to fully resolve this question.

[6] Unless otherwise noted, numbering is based on the *Lactobacillus casei* sequence.

ACKNOWLEDGMENT

We thank Linda S. Brinen for expert assistance in sample preparation and Carleton R. Sage and Janet Finer-Moore for helpful discussions throughout this work.

REFERENCES

1. Greene, P. J., Yu, P. L., Zhao, J., Schiffer, C. A., and Santi, D. (1994) *Protein Sci. 3*, 1114−6.
2. Madigan, M. T., and Marrs, B. L. (1997) *Sci. Am. 276*, 82−7.
3. Schafer, G. (1992) *J. Bioenerg. Biomembr. 24*, 525−7.
4. Herbert, R. A. (1992) *Trends Biotechnol. 10*, 395−402.
5. Bartlett, D. H. (1992) *Sci. Prog. 76*, 479−96.
6. Jaenicke, R. (1991) *Eur. J. Biochem. 202*, 715−28.

7. Fontana, A. (1991) *Curr. Opin. Biotechnol. 2*, 551−60.
8. Ludlow, J. M., and Clark, D. S. (1991) *Crit. Rev. Biotechnol. 10*, 321−45.
9. Neuhard, J., Price, A. R., Schack, L., and Thomassen, E. (1978) *Proc. Natl. Acad. Sci. U.S.A. 75*, 1194−8.
10. Tam, N. H., and Borriss, R. (1995) *Microbiology 141*, 291−7.
11. Montfort, W. R., et al. & Stroud, R. M. (1990) *Biochemistry 29*, 6964−77.
12. Matthews, D. A., Appelt, K., and Oatley, S. J. (1989) *Adv. Enzyme Regul. 29*, 47−60.
13. Perry, K. M., Fauman, E. B., Finer-Moore, J. S., Montfort, W. R., Maley, G., Maley, F., and Stroud, R. M. (1990) *Proteins 8*, 315−33.
14. Fauman, E. B., Rutenber, E. E., Maley, G. F., Maley, F., and Stroud, R. M. (1994) *Biochemistry 33*, 1502−11.
15. Hardy, L. W., Finer-Moore, J. S., Montfort, W. R., Jones, M. O., Santi, D. V., and Stroud, R. M. (1987) *Science 235*, 448−55.
16. Finer-Moore, J. S., Maley, G. F., Maley, F., Montfort, W. R., and Stroud, R. M. (1994) *Biochemistry 33*, 15459−68.
17. Knighton, D. R., Kan, C. C., Howland, E., Janson, C. A., Hostomska, Z., Welsh, K. M., and Matthews, D. A. (1994) *Nat. Struct. Biol. 1*, 186−94.
18. Schiffer, C., Clifton, I., Davisson, V., Santi, D., and Stroud, R. (1995) *Biochemistry 34*, 16279−87.
19. Hampton Research, 25431 Cabot Road, Suite 205, Laguna Hills, CA 92653-5527.
20. Jancarik, J., and Kim, S.-H. (1991) *J. Appl. Crystallogr. 24*, 409−11.
21. Condition 14: 28% PEG400, 0.1 M NaHEPES, pH 7.5, 0.2 M $CaCl_2$. Condition 15: 30% PEG8000, 0.1 M NaCacodylate, pH 6.5, 0.2 M $(NH_4)_2SO_4$.
22. Matthews, B. W. (1974) *J. Mol. Biol. 82*, 513−26.
23. Kleywegt, G. J., and Jones, T. A. (1994) *From First Map to Final Model* (Bailey, S., Hubbard, R., and Waller, D., Eds.) pp 59−66, SERC Daresbury Laboratory, Warrington.
24. Kleywegt, G. J. (1996) *Acta Crystallogr., Sect. D 52*, 842−57.
25. Cowtan, K. (1994) *Joint CCP4 and ESF-EACBM Newsletter on Protein Crystallography*, Vol. 31, pp 34−8, CLRC Daresbury Laboratory, U.K.
26. Collaborative Computational Project Number 4. (1994) The CCP4 Suite: Programs for Protein Crystallography. *Acta Crystallogr., Sect. D 50*, 760−763.
27. Navaza, J. (1994) *Acta Crystallogr., Sect. A 50*, 157−63.
28. Brünger, A. T. (1992) *X-PLOR Version 3.1. A System for X-ray Crystallography and NMR*, Yale University Press, New Haven, CT.
29. Rice, L. M., and Brünger, A. T. (1994) *Proteins: Struct. Funct. Genet. 19*, 277−90.
30. Brünger, A. T. (1996) X-PLOR Version 3.8, unpublished.
31. LaPat-Polasko, L., Maley, G. F., and Maley, F. (1990) *Biochemistry 29*, 9561−72.
32. Maley, F. Personal communication.
33. Santi, D. V. (1993) *Nucleic Acids Symp. Ser.* 103−5.
34. Carreras, C. W., and Santi, D. V. (1995) *Annu. Rev. Biochem. 64*, 721−62.
35. Kleywegt, G. J., and Jones, T. A. (1994) *ESF/CCP4 Newslet. 31*, 9−14.
36. Kleywegt, G. J., and Jones, T. A. (1995) *Structure 3*, 535−40.
37. Dev, I., Yates, B., Atashi, J., and Dallas, W. (1989) *J. Biol. Chem. 264*, 19132−7.
38. Climie, S., Ruiz-Perez, L., Gonzalez-Pacanowska, D., Prapunwattana, P., Cho, S. W., Stroud, R., and Santi, D. V. (1990) *J. Biol. Chem. 265*, 18776−9.
39. Michaels, M. L., Kim, C. W., Matthews, D. A., and Miller, J. H. (1990) *Proc. Natl. Acad. Sci. U.S.A. 87*, 3957−61.
40. Wells, J., Cunningham, B., Graycar, T., and Estell, D. (1986) *Philos. Trans. R. Soc. London A 317*, 415−23.
41. Pogolotti, A. L., Jr., Danenberg, P. V., and Santi, D. V. (1986) *J. Med. Chem. 29*, 478−82.
42. Otwinowski, Z. (1990) *The HKL Package*, (Yale University, New Haven, CT.
43. Oxford Molecular Group, Inc. (1996) Campbell, CA.
44. Sack, J. S. (1988) *J. Mol. Graphics 6*, 244−5.
45. Kraulis, P. J. (1991) *J. Appl. Crystallogr. 24*, 946−50.
46. Bacon, D. J., and Anderson, W. F. (1988) *J. Mol. Graphics 6*, 219−20.
47. Merritt, E. A., and Murphy, M. E. P. (1996) *Acta Crystallogr., Sect. D 50*, 869−73.
48. Merritt, E. A., and Bacon, D. J. (1998) *Methods Enzymol. 277*, 505−24.

BI981270L